AGU ADVANCING EARTH AND SPACE SCIENCE

Water Resources Research

RESEARCH ARTICLE
10.1029/2020WR029550

Hydraulics and Turbidity Generation in the Milandre Cave (Switzerland)

Cécile Vuilleumier[1,2], Pierre-Yves Jeannin[3], Marc Hessenauer[4], and Pierre Perrochet[1]

[1]Center for Hydrogeology and Geothermics, University of Neuchâtel, Neuchâtel, Switzerland, [2]Now at Camptocamp SA, Lausanne, Switzerland, [3]Swiss Institute of Speleology and Karst Studies, La Chaux-de-Fonds, Switzerland, [4]MFR Géologie-Géotechnique, Delémont, Switzerland

Key Points:

- Based on long-term monitoring and numerical modeling a conceptual model for turbidity generation in the Milandre karst aquifer is proposed
- Turbidity peaks originating from soil erosion (allochthonous) and from karst sediment remobilization (autochthonous) have been distinguished
- The flooding and the emptying of epiphreatic conduits are pointed out as main mechanisms for autochthonous turbidity generation

Supporting Information:

Supporting Information may be found in the online version of this article.

Correspondence to:

C. Vuilleumier,
cecile.vuilleumier@bluewin.ch

Citation:

Vuilleumier, C., Jeannin, P.-Y., Hessenauer, M., & Perrochet, P. (2021). Hydraulics and turbidity generation in the Milandre Cave (Switzerland). *Water Resources Research*, *57*, e2020WR029550. https://doi.org/10.1029/2020WR029550

Received 30 DEC 2020
Accepted 8 JUL 2021

Abstract Karst aquifers may convey significant sediment fluxes, as displayed by the intense turbidity peaks commonly observed at karst springs. The understanding of the origin of the suspended solids discharged at springs is key in assessing spring vulnerability and securing drinking water quality. The mechanisms for turbidity generation and sediment transport in karst are however difficult to investigate because of the general lack of access to the karst conduits. These processes have been examined in the Milandre Cave, which hosts a karst drain of regional importance, for more than 10 years by means of turbidity monitoring both inside and at the outlets of this karst system. Additionally, the composition of the suspended load (particle-size distribution and *Escherichia coli* content) has been monitored over the course of a flood event. These data are compared against a numerical simulation of the mean boundary shear stress inside the conduit network. The following conceptual model for sediment transport through the system is derived: during minor flood events, most of the turbidity comes from underground sediment remobilization, while during medium to intense flood events, soil-derived turbidity also reaches the spring. Hydraulics in the epiphreatic zone is tightly linked with autochthonous turbidity generation (mostly during the flooding and the flushing of conduits). In comparison, allochthonous turbidity is associated with finer particles, higher *E. coli*, and higher UV fluorescence. This improves the overall understanding of turbidity generation and could help the monitoring and forecast of pollution events at drinking water supplies.

1. Introduction

At karst springs, the suspended sediment concentration may rise quickly in response to storm events. The origin of the discharged particles and the timing of their breakthrough have been a longtime interest to karst hydrologists (see e.g., Mahler & Lynch, 1999; Massei et al., 2003; Ryan & Meiman, 1996). In particular, in the context of spring vulnerability assessment, many methods aiming at differentiating *autochthonous* (aquifer-derived) from *allochthonous* (soil-derived) turbidity have been proposed. The term autochthonous may refer to the sediment derived from carbonate dissolution (Mahler et al., 1999), in this paper it is used to describe turbidity created by the resuspension of previously deposited clastic sediment in the karst conduits. In contrast, allochthonous turbidity is composed of material eroded at ground surface (mainly from soils) and transported to the spring over the course of a single flood event. Autochthonous turbidity is generally identified by the fact that it reaches the spring before freshly infiltrated water (Fournier, Massei, Bakalowicz, Dussart-Baptista, et al., 2007; Fournier, Massei, Bakalowicz, & Dupont, 2007; Herman et al., 2008; Massei et al., 2003; Pronk et al., 2006; Schiperski, Zirlewagen, Hillebrand, Nödler, et al., 2015; Valdes et al., 2006). In a similar way, turbidity is often assumed to be allochthonous when its breakthrough is synchronous with the arrival of event water (Mahler & Lynch, 1999; Ryan & Meiman, 1996; Vesper & White, 2003).

Various physical and chemical parameters have been used to infer turbidity origin at karst springs. A sudden electrical conductivity (EC) drop, which may be indicative of freshly infiltrated water, is often considered as a good tracer for the arrival of allochthonous turbidity (Ryan & Meiman, 1996; Schiperski, Zirlewagen, Hillebrand, Nödler, et al., 2015; Valdes et al., 2006). This comes from the fact that rainwater is less mineralized than groundwater, which has been residing in the aquifer and dissolving the host bedrock for a certain time. However, this is not always the case and a decrease in the EC can also arise from a change in the relative contribution from the different subcatchments discharging to the spring (Perrin et al., 2007). As surface soils are much richer in organic content than intra-karstic sediments, natural fluorescence of dissolved and

suspended organic matter is another example of an indicator of allochthonous turbidity (Auckenthaler et al., 2002; Pronk et al., 2006). Fecal coliform concentrations at karst springs have also been of particular interest due to their sanitary implications. They are mostly issued from agriculture and/or septic tanks, that is, at ground surface or slightly below. They are frequently found in karst groundwater and springs, even in catchments fed by diffuse autogenic recharge. Several authors reported that fecal coliforms are in fact stored in soils or at the soil/epikarst interface and are released to the aquifer by flood pulses (Gunn et al., 1997; Knierim et al., 2015; Pasquarell & Boyer, 1995). The particle-size distribution (PSD) of suspended particles, although largely affected by the aquifer hydrodynamics (Atteia & Kozel, 1997; Reed et al., 2010), is in some cases useful to identify sediment sources (Lacroix et al., 2000; Pronk et al., 2007). Overall, a large panel of techniques does exist to differentiate autochthonous and allochthonous turbidity, although their applicability is generally site-specific (Schiperski, Zirlewagen, Hillebrand, Licha, & Scheytt, 2015). What stands out is that most of these methods are based solely on water quality variations at springs. The timing of their breakthrough is compared to that of turbidity in order to assess turbidity origin. However, a simultaneous breakthrough does not necessarily imply a common origin. And while many karst systems, lacking an accessible speleological network, can only be studied as black boxes, direct observations of sedimentary processes in karst conduits is also a critical tool to understand sediment transport in karst aquifers (Dogwiler & Wicks, 2004; Gale, 1984; Palmer & Palmer, 2006; Schroeder & Ford, 1983). The bridge between the observed sediment processes in karst conduits and turbidity variations at the springs seems however to be lacking in the current literature. This study aims at contributing to filling this gap. It is centered around the Milandre Cave in Switzerland, which has the advantage of hosting a cave stream that drains a catchment area of 13.3 km^2.

The present study uses the numerical model of the Milandre Cave presented in Vuilleumier et al. (2019) to link the hydrodynamics in the karst conduits with the water quality variations monitored at the Saivu spring, the main perennial outlet of the system, and at the Bâme spring, the main overflow outlet. The aforementioned parameters (EC, natural fluorescence, *Escherichia coli* concentration, and PSD) were monitored over the course of a year and, at a finer time resolution, over a single flood event of medium intensity. The variations of these parameters are compared with the simulated mean boundary shear stress in the karst conduits. An independent data set covering 10 years of monitoring of discharge and turbidity at the Saivu spring and at two stations in the Milandre Cave (Upstream Milandrine and Bure tributary, Figure 1) was also analyzed. Both data sets are used to test the conceptual model for sediment remobilization during flood events proposed in Vuilleumier (2017), which consists in an initial erosive phase, a depositional phase during the event maximum, and a secondary erosive phase during recession.

2. Study Site

The Milandre catchment is located in the northwestern part of the Jura Mountains, on the French-Swiss border (Figure 1). The system discharges primarily to the perennial Saivu spring (20–200 L/s, 373 m above mean sea level [a.s.l.]) and to the overflow Bâme spring (0–3 m^3/s, 375 m a.s.l.), which are located on the left bank of the valley of the Allaine River. The karst system is fed by a recharge area of 13.3 km^2 (Favre, 2001), which consists of a dry limestone plateau with an elevation of ~550 m a.s.l. This area is occupied by forests, pastures and cultivated lands. The recharge is purely autogenic and diffuse. The mean annual precipitation is 1,070 mm and the mean annual effective precipitation (precipitation minus evapotranspiration) is 520 mm (measured by the nearby MeteoSwiss weather station in Fahy). The aquifer consists of sub-horizontal Upper Jurassic limestone and is underlain by the Oxfordian marls, which act as a regional aquiclude (Kovács & Jeannin, 2003). As the active conduits lie almost directly above this impervious formation, there is no deep phreatic zone and the system is qualified as a shallow karst system (Perrin, 2003).

The catchment hosts a significant cave system, with a total length of 12 km of explored passages. Cave passages are mostly sub-horizontal (total elevation drop of 130 m) and some of them are organized in several levels. Most of them were explored in the 1960s. The site has been the subject of scientific studies since the early 1990s. It is of particular interest to hydrogeologists, as the main karstic drain of the catchment is accessible by caving along a length of 4 km. The perennial stream flowing in this karstic drain is called the *Milandrine* (Figure 1). Stream gauging surveys have shown that the discharge of the stream is equivalent to

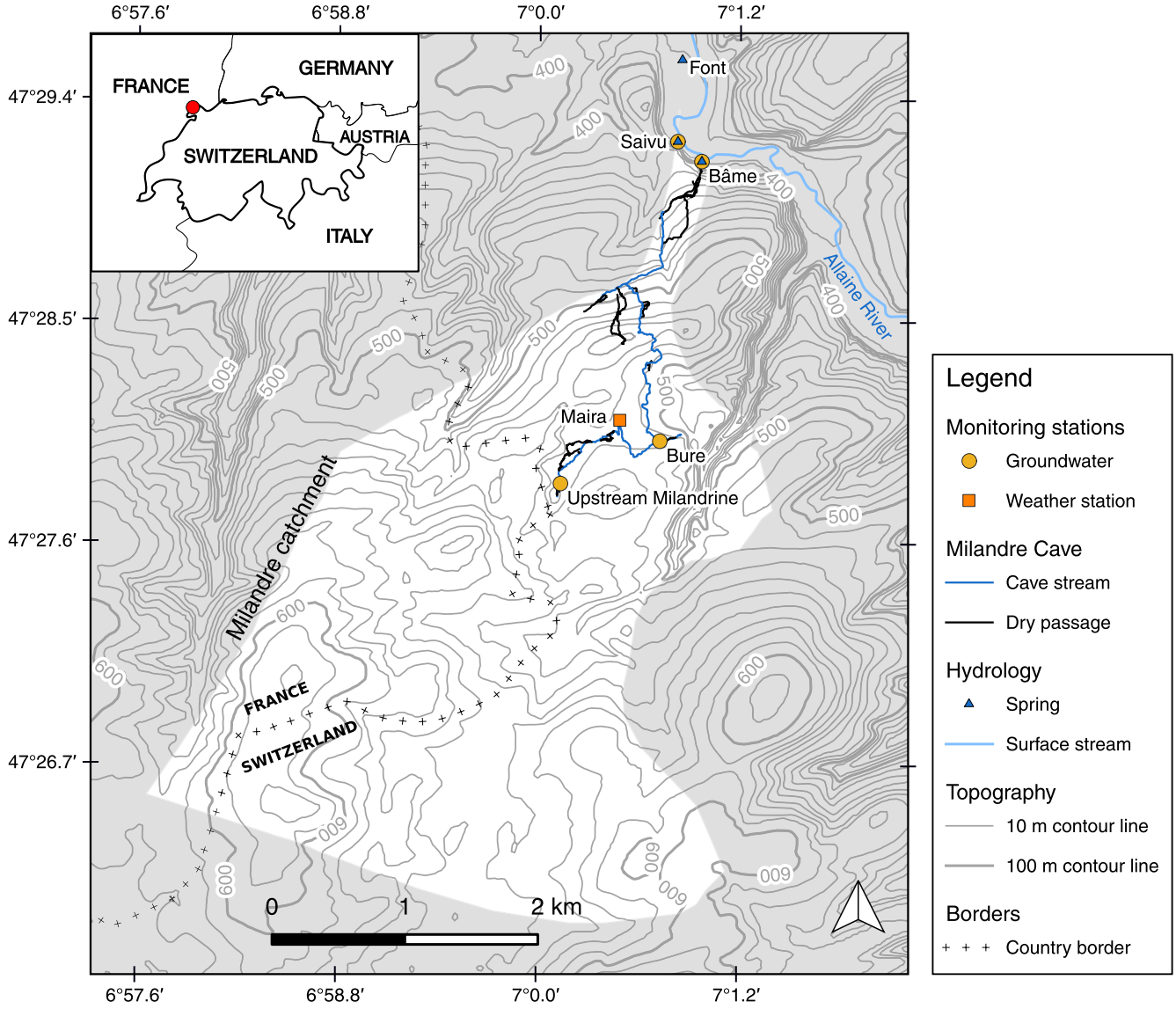

Figure 1. Situation of the Milandre Cave with the locations of the monitoring stations.

the total discharge at the outlets (Grasso & Jeannin, 1994). It is fed by two main underground tributaries, which could be explored over a length of 200 m and each contributes to almost a third of the total discharge.

The downstream part of the Milandre speleological network consists of several superimposed epiphreatic passages (epiphreatic referring to normally dry passages which become flooded during high water stage, see cross section in Figure 2). They give access to a single cave stream passage nearly 500 m upstream of

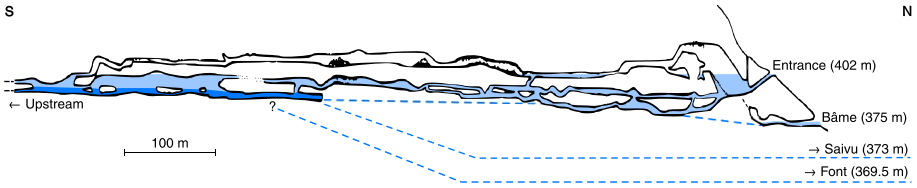

Figure 2. Cross section (vertical exaggeration 2×) of the downstream part of the Milandre Cave with inferred flow paths (dashed lines). Water level under low to medium flow conditions is shown in dark blue. Water under extreme flow conditions is shown is light blue. Cave survey from Gigon and Wenger (1986).

the springs. At its downstream end, the Milandrine reaches a sump which discharges to the perennial Saivu spring. A flow loss of the Milandrine toward the Font spring (369.5 m a.s.l.) has been identified in previous studies (Grasso & Jeannin, 1994; Vuilleumier et al., 2019). During precipitation events, the epiphreatic passages get flooded and the overflow Bâme spring starts discharging. A great length of epiphreatic passages has been explored and additional inaccessible conduits participate in groundwater flow (Vuilleumier et al., 2019). Under extreme hydrological conditions, the hydraulic head may be high enough for the cave entrance (402 m a.s.l., located above the Bâme spring) to act as a temporary outlet. Only two relatively recent instances are reported, respectively, in 2006 and in 2007.

3. Methodology

3.1. Annual and Event Monitoring of Suspended Solids at the Saivu and Bâme Springs

Discharge and water quality at the Saivu and at the Bâme springs have been monitored with a 5 min time interval from February 2015 to February 2016. The water stage has been monitored (Solinst Levelogger and Barologger Edge Model 3001, overall accuracy of 6 mm) and converted to discharge using rating curves. An existing rating curve was used for the Saivu spring and a new one was established by salt dilution gauging at the Bâme spring (Vuilleumier et al., 2019). The temperature was also measured by the Solinst Levelogger probes (resolution of 0.003°C and accuracy of 0.05°C). The EC has been monitored with HOBO U24-001 loggers (resolution of 1 $\mu S \cdot cm^{-1}$ and accuracy of 18 $\mu S \cdot cm^{-1}$). The turbidity and natural fluorescence have been monitored with GGUN-FL30 field fluorometers. Turbidity is measured in nephelometric turbidity units (NTU), which is a measure of how much light is scattered by the suspended particles in a water sample. Resolution and accuracy for turbidity measurement are 0.002 NTU and 0.5 NTU, respectively. Fluorescence is measured at excitation and emission wavelengths of 365 and 430 nm, and is used as a proxy for organic matter concentration.

Suspended solids were analyzed using two techniques: PSD of the suspended mineral grains and *E. coli* concentration. The analyses were performed on grab or automatic samples within 24 h from sampling. For the annual monitoring, samples were taken and analyzed on average biweekly. For the flood event monitoring, automatic samples were taken hourly in the early stage of the event and then bi-hourly. The PSD was measured using an Abakus mobil fluid particle counter (Klotz, Germany). Particles are sorted in 32 grain size classes between 0.9 to 139 μm. The size of the classes varies from 0.5 μm for finer particles to 39 μm for the larger ones. During the flood event, several samples were above the saturation threshold of the machine and were diluted 10–100 times in ultrapure water of total particle concentration below 300 particles per mL. For the bacterial analysis, 100 mL samples were filtered on Millipore 0.45 μm filter and then incubated for 2 h on trypticase soy agar medium at 37°C and for 22 h on tryptone Bile X-Glucuronide medium at 44°C. Annual monitoring values are given in colony-forming units (CFU) per 100 mL, which represents the number of viable bacterial cells in a water sample. During the flood event monitoring, several analyses were done on 10 mL samples due to high concentrations which lead to a saturation of the filter. Results are then normalized in CFU per mL for all the measurements of the flood event monitoring.

3.2. Long-Term Turbidity Monitoring

As part of the environmental impact study of the construction of the A16 highway, which passes over the cave, several stations for flow rate, and water quality monitoring have been set up in the Milandre system. Additionally, hourly precipitation has been monitored at the Maira weather station, located in the middle of the catchment (Figure 1). In this study, flow rate and turbidity time series recorded at a 15 min time interval from 2003 to 2015 at the Saivu and Bâme springs, at the most upstream station in the Milandrine and in the *Bure* tributary are analyzed. The location of these monitoring stations is shown in Figure 1.

Water stage was monitored with MADD probes and converted to flow rate by rating curves. MADD probes are multiparameter probes for hydrological measurements formerly provided by MADD Technologies Sàrl (Switzerland). At the Saivu spring, the turbidity monitoring is provided by a Sigrist photometer (models KTJ25 and WTM500). In the underground stream, turbidity is measured with a GGUN-FL30 field fluorometer. Due to frequent and intense turbidity events, the measurement is affected by fouling—that is,

the measuring tube gets covered by sediment, leading to the reading of turbidity being overestimated (Figure S1). The tube was cleaned on average every 3 months. A correction was applied using the turbidity drop achieved by cleaning, which can be attributed to fouling. As flood events are more frequent than probe cleaning, the total fouling after a flood event is not always known. In such cases, total fouling is assumed to be equal to the difference between the measured turbidity after the event, once stability is reached again, and the baseline turbidity signal measured when the tube is clean. Fouling is then interpolated at each time step using the assumption that the fouling rate is proportional to instantaneous turbidity (Figure S1).

3.3. Numerical Modeling

Sediment movement starts when the boundary shear stress exerted by flowing water on the channel bed exceeds a critical value which depends on the nature of the sediment. Several authors have used this approach to assess whether the erosion of previously deposited clastic sediment is likely to occur in karst conduits (Dogwiler & Wicks, 2004; Gale, 1984; Herman et al., 2012). In this study, we use the results of a numerical flow simulation to estimate the mean boundary shear stress in the conduits. The model development and performance are described in details in Vuilleumier et al. (2019) and a brief overview is presented here. The model itself and the simulation results can be downloaded at Vuilleumier (2019). The model is developed with the pipe-flow modeling software SWMM5 from the US EPA, which simulates turbulent flow in variably saturated pipes. The governing model equations are the Saint-Venant equations of conservation of mass and momentum. Head losses are computed using the Manning-Strickler formula:

$$Q = \frac{1}{n} R_h^{2/3} \left(\frac{\Delta H}{L} \right)^{1/2} A \tag{1}$$

where Q is the conduit discharge ($m^3 \cdot s^{-1}$), n the Manning roughness coefficient ($s \cdot m^{-1/3}$), R_h the hydraulic radius (m), ΔH the head loss (m), L the conduit length (m), and A the flow cross-sectional area (m^2). As most head loss in karst conduits is caused by friction along conduit walls (Bögli, 1980; Jeannin, 2001; Kaufmann et al., 2016), local singularities are not explicitly modeled and are taken into account by using a relatively high Manning coefficient. To enable a smooth transition between free-surface and pressurized flow, the model incorporates the conceptual vertical and narrow Preissmann slot to the pipe soffit.

The model is built upon a cave survey and conduits are discretized according to the survey line-of-sights which have an average length of 6.7±3.6 m. The cross sections of the resulting conduits are schematically represented as rectangular, corresponding best to the observed cross sections. Rather than using the dimensions measured at each survey station, an average height and width for each conduit are read from the hand drawn cave survey. This is to prevent a sampling bias which may arise from the fact that cave surveyors tend to avoid tight passages when they select a station location. For the Manning roughness coefficient, a homogeneous value of 0.05 $s \cdot m^{-1/3}$ is considered. This value was obtained empirically from various caves in Switzerland (see e.g., Jeannin, 2001). The model is manually calibrated by adjusting the geometries of the unexplored conduit using hydraulic head data. Hydraulic heads have been monitored at 10 locations within the cave system for several months for this purpose. Two monitoring locations have been used for the calibration and the eight remaining stations were used to validate the model. The model shows a good performance in reproducing hydraulic heads, spring discharges, and transit times (as measured with tracer tests). A flow simulation is then performed over the course of over 10 years (2004–2015) at a time step of 15 min. The cumulative discharge of the Saivu and Bâme springs, which have been monitored over this period of time, are used as the inflow applied at the upstream of the model. Here, the inflow is shifted earlier in time by 4:30 h, in order for the initial discharge increase at the Saivu spring to correspond to what was actually observed at the spring.

In a separate step which is described in Vuilleumier (2017), the flow simulation results are used to estimate the mean boundary shear stress τ_0 (N/m^2) in each conduit of the model using the following equation:

$$\tau_0 = \rho g R_h \frac{\Delta H}{L} \tag{2}$$

where ρ is the density of water ($kg \cdot m^{-3}$), g the gravitational acceleration ($m \cdot s^{-2}$), R_h the hydraulic radius (m) and $\frac{\Delta H}{L}$ is the friction slope (−). In this paper, the simulated shear stress is visually compared with the

measured turbidity curves in order to help identifying autochthonous turbidity peaks. As turbidity is caused by the suspended load, the bedload is not taken into account. Furthermore, sediment in the Milandre Cave is mostly in the silt-clay range and thus more likely to be transported as suspended load. Indeed, fine sediment accumulation is observed on the stream banks and on the walls in active conduits (Figure S19). In Vuilleumier (2017), the critical shear stress for these sediments has been estimated at around 0.65 N/m^2

4. Results and Interpretation

4.1. Annual Suspended Solids Monitoring

The results of the annual monitoring of the Saivu and Bâme springs are plotted in the supporting information (Figures S2 and S3) and briefly commented in this section.

At the Saivu spring, the discharge varied between 15 and 200 L/s. The lowest discharge is observed during the end of October and in November, after particularly dry summer and fall seasons. The highest discharge peaks were reached during flood events in the spring and in the winter. The discharge threshold of about 90 L/s, above which the Bâme starts to flow, is well visible in the data. Indeed, the flow rate was between 80 and 100 L/s during one third of the total monitoring period. In contrast, the Bâme spring was dry for half of the monitoring period, and some of its discharge peaks are equal to or greater than 2,000 L/s.

Recharge events are also associated with changes in water quality. At the Saivu spring, the EC has a baseline value of ~610 $\mu S \cdot cm^{-1}$ and decreases by roughly 100 $\mu S \cdot cm^{-1}$ during flood events. The temperature is often stable at 10.2°C and generally, but not always, increases during high flow. The maximum amplitude of increase is 0.25°C. Turbidity varies between 1 NTU during stable flow conditions to 150 NTU during the most intense events. Fluorescence also increases during flood events, going from 1 mV to maximum 6 mV. Fluorescence peaks are wider and smoother than turbidity peaks. Physico-chemical parameter variations at the Bâme spring are in line with those of the perennial spring, except for water temperature which is partially affected by sunlight exposure.

Figure S4a shows the bin size normalized PSD for each sample taken during the annual monitoring. On average, 95% of the counted particles are smaller than 3.4 μm and particles seldom exceed a size of 70 μm. Accounting for both springs, the total number of suspended particles measured by PSD analyses (0.9–139 μm) on biweekly samples lies between $7.8 \cdot 10^3$ and $5.9 \cdot 10^5$ particles per mL (Figures S2 and S3). The geometric mean is of $3.9 \cdot 10^4$. *E. coli* was detected in each sample, with concentrations varying between 2 to $6 \cdot 10^3$ CFU per 100 mL and a geometric mean of 145 CFU per 100 mL.

These variations by several orders of magnitude, both in suspended particles and fecal bacteria concentrations, appear to be largely influenced by the hydrodynamics of the karst system. In a log-log space, the correlation coefficient of particle concentration versus total discharge is 0.76, and 0.52 for *E. coli* concentration versus total discharge. At this sampling resolution, no seasonal patterns are visible. It rather seems that there is a constant availability in particles and fecal bacteria and that their fluxes are controlled by the hydrodynamics of the system. Regarding fecal bacteria, they are likely released by agriculture. Both pastures and cultivated areas are present in the Milandre catchment. Fecal bacteria input is thus expected to follow a seasonal pattern, as manure spreading is allowed only during the growth period—on average, from March to early November. As *E. coli* is present at the spring all year round, it is likely that a storage exists and that it is flushed toward the aquifer by storm events, as suggested by previous authors (Gunn et al., 1997; Knierim et al., 2015; Pasquarell & Boyer, 1995).

4.2. Monitoring of Suspended Solids During an Event

4.2.1. Event Description

To monitor the evolution of suspended matter content at the scale of a flood event, frequent samples (hourly to bi-hourly) were taken throughout an event in November 2015 (Figure 3). Before the rain, low flow conditions prevailed in the aquifer, with a stable discharge of 22 L/s at the Saivu spring and a dry Bâme spring. At the Maira weather station, rainfall started early in the morning on November 20 (Figure 3a). Two rainfall pulses occurred throughout the day and in the following night, totaling 50.5 mm. The Fahy weather station

10.1029/2020WR029550

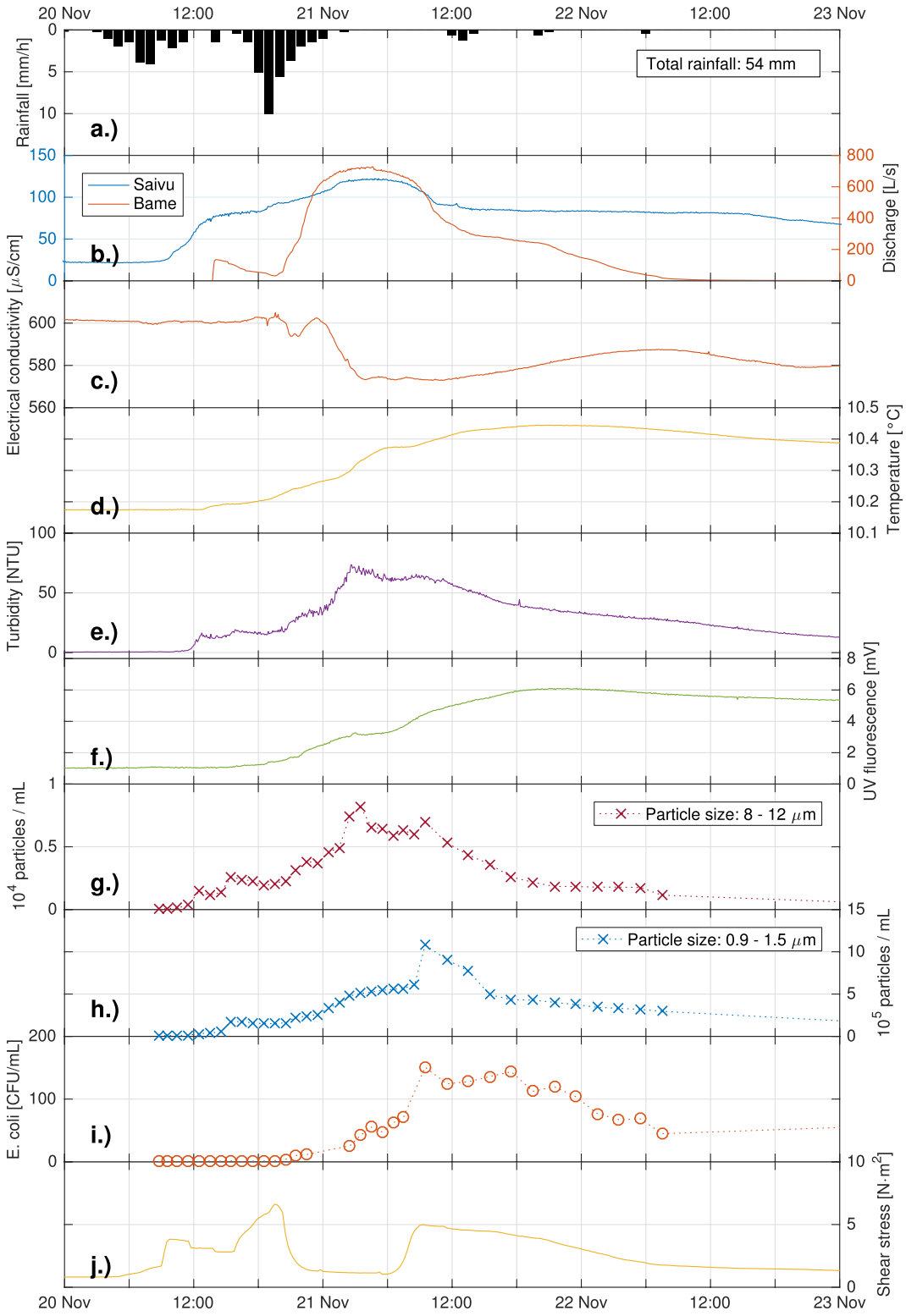

Figure 3. Flood event monitoring at the Saivu spring: rainfall (a), spring discharge (b), electrical conductivity (c), temperature (d), turbidity (e), natural UV fluorescence (f), suspended particle concentration (8–12 μm (g) and 0.9–1.5 μm (h)), *Escherichia coli* concentration (i) and shear stress in the underground stream as computed by the hydraulic model (mean value of all the stream conduits) (j).

recorded 50 mm of total and effective precipitation for the same time period. The discharge started to increase at 9:00 at the Saivu spring and peaked at 122 L/s at 5:00 the next day (Figure 3b). The Bâme spring started to flow at 14:00, November 20, and reached a maximum discharge of 725 L/s at 16:00, November 21. Due to a failure of the automatic sampler at the Bâme spring, only the samples taken at the Saivu spring are discussed hereafter.

4.2.2. Interpreting PSD Data

Figure S4b shows the PSD for each sample taken during the November 2015 flood event monitoring. Particle concentrations are generally slightly higher than those measured during the annual monitoring (Figure S4a) and larger particles are relatively more abundant. On average, 95% of the particle were smaller than 5.4 μm. To try to extract information from the PSD data, the relationships between particle-size class concentrations and other variables are investigated. Figure S5a shows the correlation coefficient and the coefficient of determination between the total discharge (sum of Saivu and Bâme springs) and the particle concentration for 24 size classes (0.9–35 μm) throughout the flood event. Size classes above 35 μm are not considered due to very low particle counts, reaching zero in some samples. Log10 values are considered for particle concentrations, as they have a lognormal distribution. Although every class between 0.9 and 35 μm is well correlated with discharge (>0.5), a maximum of 0.95 is reached at classes 8–9, 9–10, 10–11, and 11–12 μm. They also have a high coefficient of determination of 0.9. Those four classes are thus mainly hydrodynamically controlled particles and are grouped together in Figure 3g. Figure S5b shows the correlation coefficient and the coefficient of determination between *E. coli* and particle size class concentrations. Log10 values are considered for each pair of variables. The smallest and most abundant particles (0.9–1.5 μm) are less correlated with discharge than with *E. coli* concentration. The correlation coefficient is of 0.89 for 0.9–1.5 μm particles and decreases gradually for larger particles. 30–35 μm particles are virtually not correlated with *E. coli* concentration (0.14). Similarly, the coefficient of determination goes from 0.79 (0.9–1.5 μm) to 0.02 (30–35 μm). As *E. coli* bacteria typically have a size of 1 μm, a high correlation with 0.9–1.5 μm is expected. This size class is thus selected as a variable highly correlated with *E. coli* concentration and its concentration evolution is plotted in Figure 3h.

4.2.3. Suspended Solids Evolution

Figure 3 shows the evolution of 10 variables throughout the event. At the spring, discharge is the first parameter to respond, around 9:00 on November 20. Turbidity starts to increase 3 h later. As EC and temperature are stable, this initial turbidity increase is likely caused by intra-karstic sediment remobilization. Both UV fluorescence and *E. coli* concentration stay at their baseline value at this stage, which further confirms the arrival of autochthonous turbidity. At the same time, a stepwise increase in larger (8–12 μm) particles occurs, while finer (0.9–1.5 μm) particle concentration is stable. This is an indication that autochthonous turbidity is characterized by a relatively large grain size. Turbidity has a stable value around 15 NTU for the next ~7 h.

Around 21:00, as the Saivu spring discharge continues to rise, turbidity increases further. Simultaneously, UV fluorescence and *E. coli* concentration also rise, indicating the presence of allochthonous turbidity. At this stage, there is probably a mix of autochthonous and allochthonous turbidity at the spring. Turbidity reaches its peak value of 73 NTU at 02:30 on November 21, and stays at a high level until 12:00. PSD and *E. coli* data reveal more information on this high turbidity stage. The peak in larger particles was measured at 3:30, almost at the same time as the turbidity peak. Fine particles, on the other hand, peak several hours later, at 9:30, simultaneously with *E. coli* bacteria. Since 8–12 μm particles started to increase early in the event, they are considered to indicate the presence of autochthonous turbidity. The larger particle (8–12 μm) peak is thus interpreted as the peak contribution of autochthonous turbidity. Because of its simultaneity with the fecal bacteria, the fine particle peak is interpreted as the allochthonous turbidity peak. Shortly after, at 11:00, turbidity starts to recede, together with both fine and larger particles.

4.2.4. Indications From the Hydraulic Model

The PSD and *E. coli* data suggested that the turbidity pulse during the November 2015 flood is in fact an overlay of an autochthonous turbidity peak and an allochthonous one, the former slightly preceding the latter. This hypothesis can be tested against the hydraulic numerical model of the downstream part of the karst system (see Section 3.3 and Vuilleumier et al., 2019).

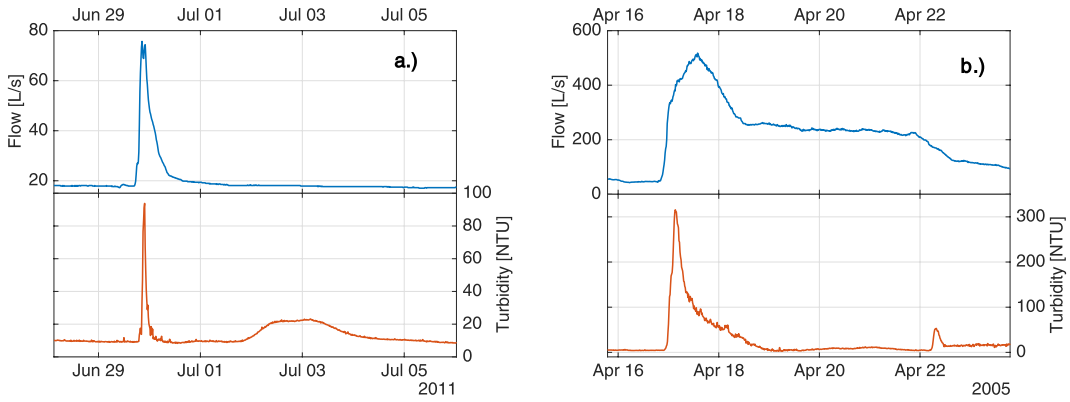

Figure 4. Flow rate and turbidity variations during two flood events (moderate (a) and intense (b)) at the upstream station in the Milandrine underground stream.

Figure 3j shows the mean boundary shear stress in the underground stream throughout the flood event as computed by the model. For this plot, first, all conduits of the model which are part of the perennial cave stream are selected. The mean boundary shear stress is then averaged over all of those conduits for each simulation time step.

Mean boundary stress in the conduits shows a two-step increase in the initial stage of the event. This is probably caused by the two phased rainfall pulses (Figure 3a). Between 10:00 and 16:00 on November 20, the average shear stress plateaus around 3–4 $N{\cdot}m^{-2}$, which is enough for significant erosion. This is in line with the initial turbidity plateau at the Saivu spring, which was interpreted as autochthonous in the previous section. The model predicts a maximum shear stress of 7 $N{\cdot}m^{-2}$ at 19:30. This corresponds to the time where the underground stream has the strongest erosive power. Taking into account the fact that the model predicts a 9 h transit time from the underground stream to the outlet at this stage of the event, this is compatible with the autochthonous peak observed at 3:30 at the spring. The shear stress peak is quite narrow and shear stress rapidly decreases although the flow rate is still increasing. Again, this does not contradict the arrival of the allochthonous peak detected at 9:00 at the spring, since it corresponds to a period of relatively low shear stress in the conduits. However, since the model includes only the downstream part of the conduit system and does not simulate the transfer of particles, it cannot give further insight into allochthonous turbidity transport. Later on, at 7:00, a secondary shear stress peak is predicted by the model at the onset of the event recession—as the system is draining, the stream regains erosive power. This is in line with the results presented in Vuilleumier (2017): at the sedimentation monitoring station, where on several instances, erosion was observed in the lower part of the conduit while deposition was visible in the upper part. This can be understood in the sense that the flow velocity in the conduits is higher during the flooding and draining of the system than at the flood peak, because back-flooding of the conduits induces a significant increase in flow cross section. Hydraulic head monitoring in Vuilleumier et al. (2019) indeed showed relatively low gradient in the karst network at the event maximum, confirming this back-flooding. However, no evidence for a secondary autochthonous peak was found at the spring through the flood event monitoring.

4.3. Long-Term Turbidity Monitoring

4.3.1. Milandrine Upstream Station

The monitoring station at the upstream end of the Milandrine is of interest with regard to event scale turbidity variations for several reasons. In some instances, anomalous wide turbidity peaks appear 1 or 2 days after recharge events and last for ~2 days. These were not seen at the Saivu spring. Figure 4a shows an example of one such event. They are of moderate intensity and occur during otherwise low flow conditions. They are characterized by a first narrow turbidity peak, lasting a few hours, which is simultaneous with the discharge peak. The secondary turbidity peak is of smaller intensity, lasts for 1–2 days and occurs once the flow rate is back to its pre-event value. They do not appear systematically and seem to be more frequent

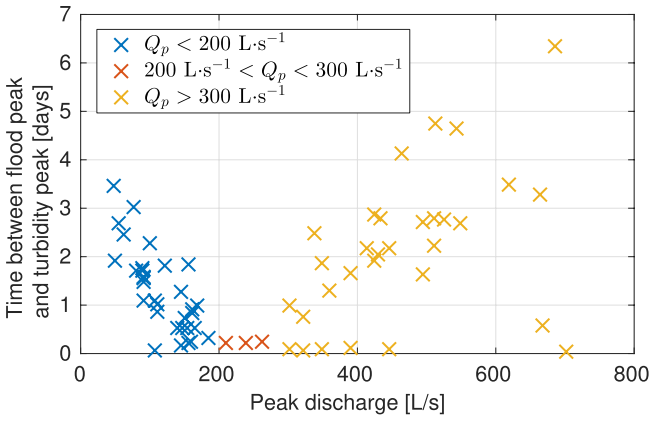

Figure 5. For 66 events recorded at the upstream Milandrine station, the event peak discharge (Q_p) is plotted against the time between the peak discharge and the secondary turbidity peak.

in the summer. Pronk (2008), analyzing two such events by monitoring turbidity and TOC, suggested that the wide turbidity peak is caused by the arrival of allochthonous sediment.

In the 10-year time series of flow rate and turbidity, another type of secondary turbidity peaks appears. They are produced during more intense flood events and have the distinctive feature of appearing during flow recession. An example is shown in Figure 4b. Again, these secondary peaks are less intense than the primary ones, but they are relatively short, lasting for a few hours. And, in contrast to the first type of secondary peaks, they can occur up to 1 week after the mean discharge peak. Their common features are that they appear when the stream discharge starts to recede after a several days period, where it had a stable value around 200–300 L/s. This flow rate threshold is visible in the flow relative frequency distribution, which has a local maximum around 270 L/s (Figure S6a). It has already been described by Pantillon (1993) who explained it by the presence of a scree at the upstream end of the Milandre Cave network. This scree impedes groundwater flow and induces an increase in hydraulic head on its upstream side, thus acting similarly to a dam.

In an attempt to gain understanding on the mechanisms controlling the appearance of secondary turbidity peaks, discharge and turbidity time series were analyzed and the following variables were defined for each flood event displaying several turbidity peaks: initial discharge, peak discharge, primary turbidity peak, and secondary turbidity peak, as well as the arrival times of the initial flow increase, of the discharge peak, and of the primary and secondary turbidity peaks. If the event displayed more than two turbidity peaks, the first peak is always considered the primary peak, and the following ones are successively regarded as secondary peaks, so that one flood event may appear several times in the data set. The total number of events is 66 and they are depicted in the supporting information (Figures S7–S17). No strong relationship emerges between turbidity peak intensity and flow rate. However, an interesting pattern appears when plotting discharge peak value (Q_p) versus the time between the flood peak and the secondary turbidity peak, as shown in Figure 5. Three groups of events can be distinguished:

1. Q_p < 200 L/s The time between the flood peak and the secondary turbidity peak decreases when peak discharge increases
2. 200 L/s < Q_p < 300 L/s No visible effect of the peak discharge on the time between flood and secondary turbidity peak
3. Q_p > 300 L/s The time between the flood peak and the secondary turbidity peak increases when peak discharge increases

The first category of events is compatible with the advection of soil sediment from the surface—the higher the flow rate, the faster the flow velocities. The wide shape of the peak also indicates a relatively long transport, which allows some dispersion. This implies that the primary turbidity peak is caused by sediment remobilization in the aquifer, meaning that an underground sediment accumulation zone also exists upstream from the known cave stream. For peak discharge nearing 200 L/s, the delay between the flood peak and the secondary turbidity peak approaches zero. Autochthonous and allochthonous turbidity probably overlap at higher discharge, as observed at the spring in Section 4.2.3. However, this interpretation does not hold for the third category of events. More importantly, the secondary turbidity peak during those events is associated with the onset of flow recession (Figure 4b and Figures S4–S14). The higher the flood peak, the longer before flow recession, explaining the positive relationship between peak discharge and the time between flood peak and the secondary turbidity peak. As seen in Section 4.2.4, these peaks could be issued by a secondary erosive phase initiated by the flushing of the epiphreatic zone during flow recession.

4.3.2. Saivu and Bâme Springs

To analyze the turbidity variations at the Saivu spring, the total discharge of the Bâme and Saivu springs is considered, as it represents almost the total discharge of the system. The turbidity response at the Saivu spring is often plurimodal and cannot be easily separated in different peaks such as at the upstream end of

the Milandrine (Figure S18). Indeed, while the turbidity observed at the upstream end of the Milandrine likely contributes to the turbidity at the Saivu spring, other turbidity inputs reach the cave stream: the *Bure* and the *Droite* tributaries, which each contribute to almost a third of the total discharge of the Milandrine, and the downstream epiphreatic zone, where previously deposited sediment is remobilized. As a result, the turbidity signal at the Saivu spring is a superimposition of these different contributions. Some insight can be gained into these processes by comparing the turbidity signal in the underground network and at the spring, as done in Figure S18. In this figure, two events belonging to the data set described in the previous section are shown. At the upstream station, these events generated a primary turbidity peak during the flood event, which is interpreted as autochthonous, and a secondary, much dispersed peak which is interpreted as allochthonous. The turbidity signal in the *Bure* tributary is analogous to the upstream Milandrine signal, although the secondary peak is less delayed. At the Saivu spring, the primary turbidity peak has an irregular shape. No secondary peak is observed for the event represented in Figure S18a, which is of low amplitude with a peak discharge at the springs of less than 200 L/s. For the event of Figure S18b, of slightly higher amplitude with a peak discharge of 350 L/s at the springs, a very dispersed secondary turbidity peak is detected at the spring 2 days after the flood peak. Four other events of the same data set, with peak discharges between 300 and 400 L/s (09.2005, 05.2006, 06.2008, 03.2011), displayed a similarly delayed and flattened secondary turbidity peak appearing 1 or 2 days after the flood peak. The proposed interpretation of the turbidity response of the Saivu spring to low amplitude events is that the primary turbidity peak is composed of a superimposition of autochthonous turbidity contributions from the three subcatchments and from the downstream epiphreactic zone, while the allochthonous turbidity is mostly redeposited in the conduit network or too dispersed to be detected at the spring.

Similarly to the upstream Milandrine, recession turbidity peaks may be observed during major flood events ($Q_p > 1\,m^3/s$) at the Saivu spring. They were already reported by Rodriguez (1996), who found that they regularly appeared when the recession starts to slow down around 600 L/s. Indeed, similarly to the upstream Milandrine, the total spring discharge displays a threshold during recession, as evidenced by the local maximum at 585 L/s in the flow frequency distribution in Figure S6b. It is also well visible during most of the events depicted in Figure 6. Looking through the turbidity time series from 2003 to 2015, secondary peaks as described by Rodriguez (1996) were again found. They are marked with dashed vertical lines in Figure 6. But even more delayed secondary peaks may get to the spring: they arise after the ~600 L/s threshold, when flow rate further drops. They are marked by dotted vertical lines in Figure 6. The relationship between secondary peak occurrences and the hydrograph seems consistent between events. Their absolute and relative intensity however varies greatly. In both cases, they appear to be triggered by a sudden decrease in flow rate, similarly to the secondary turbidity peaks found at the upstream Milandrine station during major flood events. Again, this erosive phase may be caused by the emptying of epiphreatic conduits.

The hypothesis that those recession turbidity peaks have an autochthonous origin can be tested against the hydraulic simulation produced by the numerical model. As performed for the November 2015 flood event analysis (Section 4.2.4), the mean boundary shear stress simulated in the conduits for most of the events of Figure 6 is plotted on the same figure. In contrast to Figure 3j, the average is computed from the epiphreatic conduits—that is, all the conduits in the model, excluding cave stream conduits and dry conduits. During the main flood peaks, there may be one or two shear stress peaks. Indeed, the pattern simulated for the November 2015 flood event, that is, a shear stress peak during the onset of the event, followed by a phase of low shear stress during high stage, again followed by a shear stress peak, is found again during the events c, f, g, h, j, and l, the main flood peak (discharge greater than 1 m^3/s) of several events (Figures 6c, 6f, 6g, 6h 6j and 6l). This corresponds to the flooding and the emptying of the upper epiphreatic passage flowing to the Bâme spring (~ 390 m a.s.l., see Figure 2). The absence of this pattern during the other events depicted in Figure 6 is here attributed to a faster sequence of onset and recession phases. The simulated shear stress peaks during the flood peak are however not linked in an obvious way to the first type of recession turbidity peaks (dashed lines in 6). In contrast, the second type of recession turbidity peaks, which appears after the flow threshold at ~585 L/s (dotted lines in Figure 6), are systematically associated with a marked and lasting rise in shear stress in the epiphreatic network, which corresponds to the emptying of lower epiphreatic passage flowing to the Bâme spring (~382 m a.s.l., see Figure 2). This further supports the hypothesis of autochthonous turbidity production by conduit drainage during flow recession. It is interesting to note, however, that not each of such shear stress rises produce a detectable turbidity peak at the Saivu spring. The

10.1029/2020WR029550

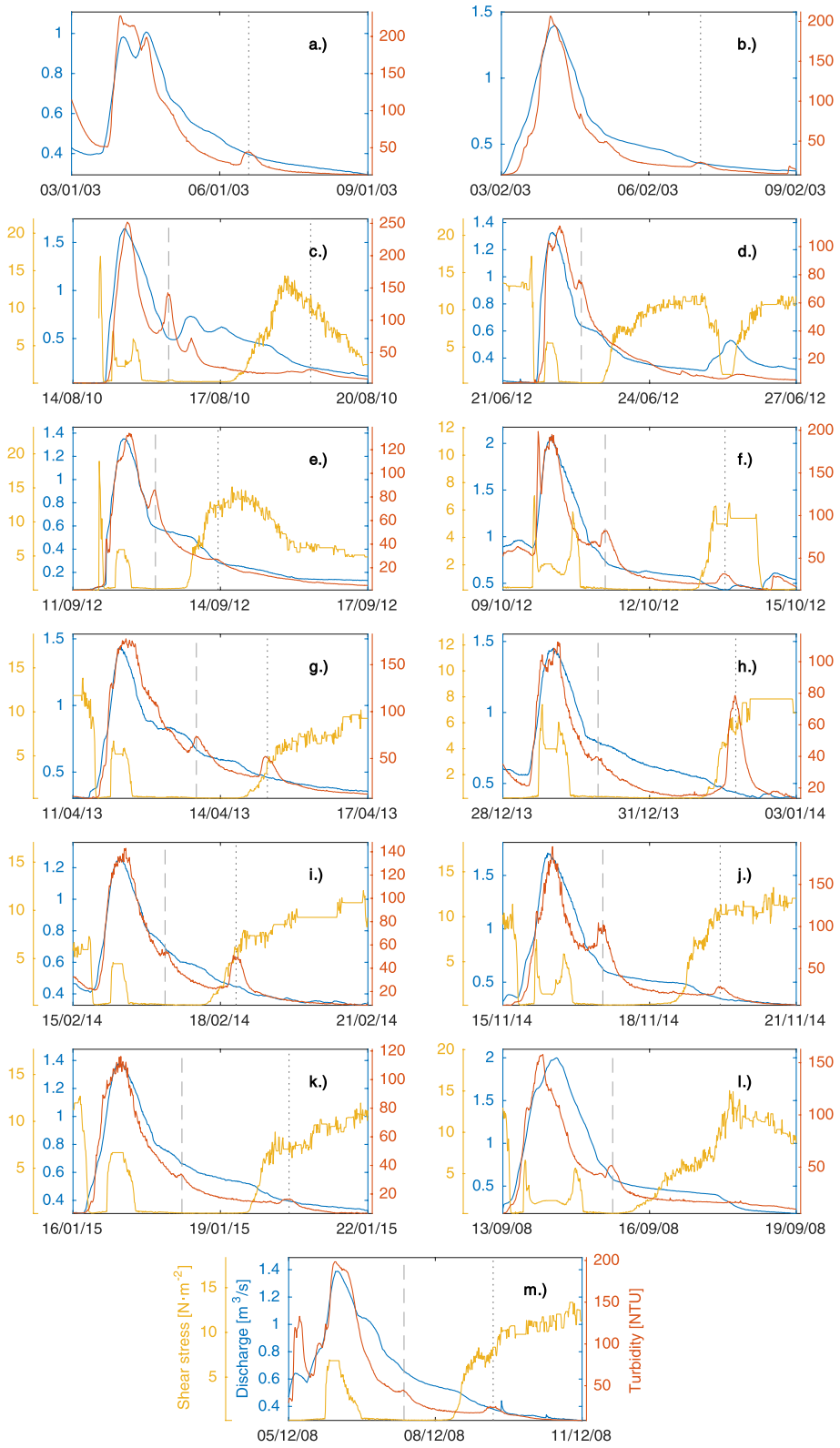

Figure 6. Discharge (blue), turbidity at the Saivu spring (orange), and simulated shear shear in the conduit system during a selection of major flood events (a to m). The discharge is the cumulative Bâme and Saivu flow rates. The shear stress is the mean value at each simulation time step over all the epiphreatic conduits of the model.

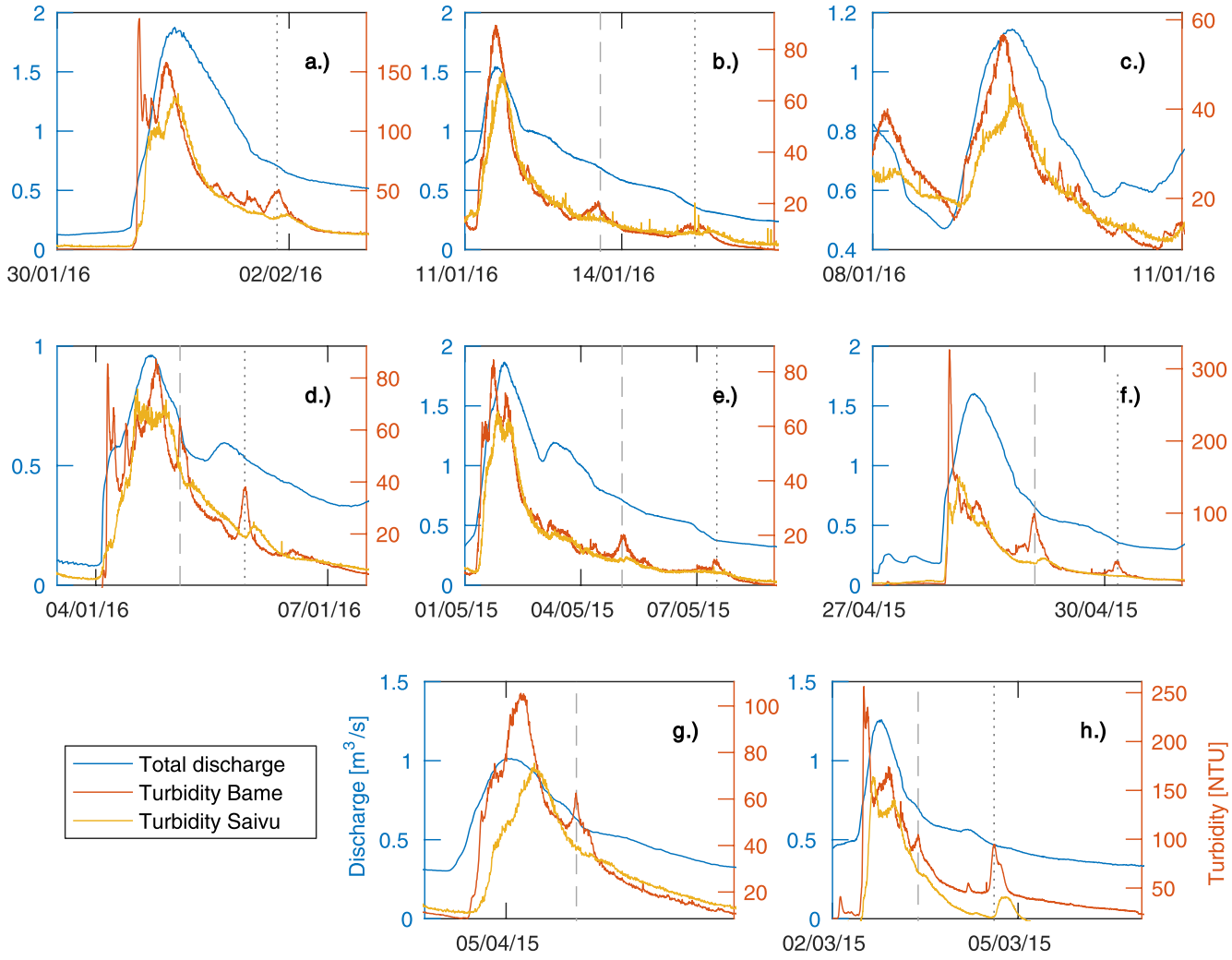

Figure 7. Turbidity variations during major flood events at the Bâme and Saivu springs (a to h). The discharge is the cumulative Bâme and Saivu flow rates. Recession turbidity peaks are marked by dashed and dotted lines.

reason for this is not clear at this point. Maybe this is due to the sediment being redeposited before reaching the spring, or it is a consequence of the simplifications of the modeling approach. Also, similar to what was found at the Milandrine station, the intensity of the recession turbidity peaks varies greatly.

These findings can be compared to the turbidity signal at the Bâme spring, which has been monitored from February 2015 to February 2016. Eight major events ($Q_p \geqslant 1\,\mathrm{m}^3/\mathrm{s}$) are depicted in Figure 7. Turbidity values during flood events are generally higher at the Bâme spring than at the Saivu spring. During the flood peak, the turbidity signal is very chaotic, often displaying several rapid increases followed by similarly rapid decreases which do not appear at the Saivu spring. These extra peaks are thus attributed to sediment remobilization in the downstream part of the system, since the Bâme spring is the outlet of the epiphreatic conduits. The recession turbidity peaks found at the Saivu spring, both before the flow rate threshold (dashed lines in Figure 7) and after (dotted lines), are still observed and are even more frequent compared to the perennial spring. This confirms that these peaks are generated in the downstream part of the karst system.

5. Discussion

In this study, turbidity variations at the scale of flood events in the Milandre system have been investigated and mechanisms for the generation of turbidity are proposed. Three different data sets have been analyzed: (a) one flood event monitored for many parameters at high time resolution at the two main springs of the Milandre hydrogeological system, (b) multiparameter data including turbidity and microbiology along 1 year, and (c) 10 years of discharge and turbidity data at the upstream end of the cave stream and at the perennial spring. These data sets are analyzed by considering observations and modeling of the hydraulics of flow within the conduit network presented in Vuilleumier et al. (2019). This model provides 10 years of time series of flow velocities, transit time and shear stress in the cave system. These data sets and modeling represent a solid background for interpreting the origin of turbidity peaks observed at the springs. Time series show that most flood events are accompanied with several turbidity peaks, usually one main peak during the rising of the discharge, and one or two secondary peaks during recession stages.

The numerical model does hold certain limitations: conduits are considered as one-dimensional elements, neglecting the velocity and shear stress distribution in the cross section, and the boundary shear stress formulation used is mostly valid under unsaturated flow conditions. The model is however highly refined in comparison to other models of karst systems at the catchment scale in the current literature (Chen & Goldscheider, 2014; Gabrovšek et al., 2018; Kaufmann et al., 2016; Wu et al., 2008). As for the calculation of the shear stress, it has rarely been applied to karst conduits, with the exception of Dogwiler and Wicks (2004). They provided a very detailed characterization of the sediment (grain size, critical shear stress), but in terms of hydraulics, their data are limited to water stage monitoring. The flow simulation used in this study is thus unique and provides interesting insight, especially when compared to the turbidity curves.

From the flood event monitored in November 2015 for PSD, *E. coli* and water quality we could identify a mixed contribution of autochthonous and allochthonous sediment to the spring turbidity. This flood event was of medium intensity, with a cumulative peak discharge at the springs of 850 L/s and total effective precipitation of 50 mm. Allochthonous turbidity was identified by a simultaneous increase of 0.9–1.5 μm particles and *E. coli* concentration, and high UV fluorescence. In November 2015, these parameters started to rise nearly 7 h after the beginning of the first rise of the discharge rate. This is expected to correspond to the arrival of soil and epikarst waters. This is fully compatible with results of Perrin et al. (2007), who made a similar observation concerning variations of the EC at the spring. Subsidiary EC peaks were very well explained by the arrival of soil and epikarst water from the respective tributaries monitored in the cave. These results are also in line with the conceptual model of the system previously proposed by Perrin et al. (2003). Through stable isotope analyzes of rainfall and cave stream water, they stated that freshly infiltrated water may reach the saturated zone over the course of one event when infiltration is greater than 15–20 mm. As the event observed in this study reached 50 mm of rainfall, the arrival of fresh water at the spring can be expected. Also, the fact the allochthonous sediment has a finer grain size than autochthonous sediment is consistent with the fact that it has been transported over longer distances, thus there is a higher probability for the potential larger allochthonous particles to have settled before reaching the spring.

Autochthonous turbidity was characterized in time series by a relatively high content in 8–12 μm particles, low UV fluorescence and low *E. coli* concentration. In November 2015, turbidity and 8–12 μm particles started to rise nearly 2 h after the beginning of the first rise of the discharge rate. This is consistent with the hydraulic model (Vuilleumier et al., 2019) which shows a sharp increase of the mean boundary shear stress in the conduit in the initial stage of the event. In Vuilleumier (2017), this has been deemed as enough to initiate sediment entrainment. The transit time measured in the phreatic zone by tracer tests also shows a good match between the simulated erosive phase and the observed autochthonous peak at the spring. This confirms that the first peak is mainly related to autochthonous particles, already present in the karstic system before the flood (erosion of cave sediments). The model further predicts a decrease in boundary shear stress at the event maximum, which does not contradict the observed arrival of allochthonous turbidity at that time. During flow recession, the model indicates a secondary maximum in shear stress, which is caused by the emptying and "washing" of the conduits. It seems that no effect of this potential secondary erosive phase was seen in the suspended sediment during the flood in November 2015. However, it can be observed that particles and *E. coli* both increase shortly after this rise of shear stress. An erosion of the sediments just deposited during the period with low shear stress at discharge peak could be an explanation for this rise.

Turbidity generation in the Milandre system has been further investigated by comparing 10-year time series of turbidity monitored at the Saivu and Bâme springs with the simulated shear stress in the conduit network. The predicted behavior (turbidity peak corresponding to the increase of shear stress during recession) was observed for 21 events during which an upper level of karst conduits (epiphreatic conduits) was flooded and subsequently drained.

Finally, 66 flood events which generated a multi-peak response in turbidity at the upstream Milandrine monitoring station were analyzed. For minor flood events (peak discharge in the upstream of the Milandrine < 200 L/s), an autochthonous turbidity peak occurs during the flood event, and a distinct, wider and longer allochthonous peak may be observed up to several days after the event, once the flow rate is back to its pre-event value. The delay between the discharge peak and the secondary turbidity peak consistently decreases as the peak discharge value increases. For more intense flood events (peak discharge in the upstream of the Milandrine > 200 L/s), the arrival of allochthonous turbidity overlaps that of autochthonous turbidity. Again, this can be compared with the observations of Perrin et al. (2003) who sampled the cave stream at this location for stable isotope analyzes. For a minor flood event (peak discharge of 180 L/s), they found that no freshly infiltrated water reaches the cave stream over the course of the event. This is in line with the delay observed in the breakthrough of the allochthonous turbidity peak, which may arrive several days after the discharge went back to its pre-event value. Conversely, evidence for freshly infiltrated water in the cave stream was found during two more intense events (peak discharge in the upstream of the Milandrine of 260 and 400 L/s), meaning that the direct transport of soil sediment is indeed possible for events of similar intensity. Furthermore, recession turbidity peaks at the upstream Milandrine station have also been pointed out in this study. They are simultaneous with the emptying of an epiphreatic level and the subsequent increase of the shear stress in those conduits.

The turbidity signal in the upstream Milandrine was compared to the one at the Saivu spring for a series of minor flood events (peak discharge at the Saivu and Bâme spring ≥ 500 L/s). This leads to the conclusion that most of the allochthonous sediment is deposited in the phreatic zone and does not reach the spring. In some cases, a very weak and dispersed peak was observed 2 days after the event. The turbidity signal during such events has an irregular shape with several secondary maximas. The turbidity signal at the Saivu spring during minor events is thus thought to be the superimposition of different autochthonous contributions coming from the respective tributaries and from the downstream part of the Milandre stream (epiphreatic zone).

This event scale pattern of erosion, with an initial erosive phase, followed by a quiescent phase at high stage, itself followed by a secondary erosive phase during recession, as predicted by the model, is also in agreement with the observations made at the sedimentation monitoring station in the main conduit along the cave stream (Vuilleumier, 2017). During this experiment, 12 sedimentation plates have been set up at different heights above the cave stream and inspected at 3 months intervals for 10 years. Erosion was only observed on the lowest sedimentation plates, meaning it occurred during relatively low water stages. In constrast, the upper sedimentation plates, which are flooded during the event maximas, showed significant sediment accumulation.

This study sheds new lights on the origin of turbidity and on the transport of particles through karst aquifers. Papers published before 2006 rarely present turbidity curves with a high resolution measured simultaneously to other tracers typical for the arrival of surface or soil water. Several authors postulated the arrival of both autochthonous and allochthonous turbidity.

Ryan and Meiman (1996) show the effect of lag time related to the arrival of what they assume to be allochthonous turbidity. In fact, they do not provide any indication about autochthonous turbidity, and the flood events they analyzed were potentially too low to have produced a significant autochthonous turbidity peak. Their criteria for determining the origin of the turbidity are not very well explained and not supported by direct observations and/or by modeling. The same remark applies to Mahler and Lynch (1999), and somehow to Vesper and White (2003). These studies were more focused on the analysis of suspended matter composition. The time resolution of their time series is therefore limited by the sampling frequency, making it difficult to compare their results with the conceptual model presented in this study.

Pronk et al. (2006) observed a sharp turbidity peak early at the beginning of the discharge peak and they clearly postulated that it originated from the remobilization of sediments previously present in the conduit network. They also noticed the presence of a very similar peak during the recession of flow. About this peak, they write: "As this signal occurred during a period of decreasing flow rates, it cannot be explained by remobilization of sediments inside the conduit network." Based on our observations in Milandre, we can now say that this peak is very probably also autochthonous. Herman et al. (2008) provide good indications about turbidity peaks produced by the remobilization of sediments in cave passages upstream from the spring they investigated. It was clearly postulated by the authors, but it was not demonstrated by a complete analysis of the hydraulics of flow, as carried out in our study. Unfortunately, in their study, the sampling was not long enough to see if a secondary peak occurred during the flow recession. Valdes et al. (2006), Fournier, Massei, Bakalowicz, Dussart-Baptista, et al. (2007), and Fournier, Massei, Bakalowicz, and Dupont (2007) applied another type of approach, more oriented toward signal analyses. Their findings, however, are compatible with ours, as they could identify periods dominated by autochthonous turbidity and others by allochthonous turbidity. As their approach is less based on the physics of flow and transport than ours, a direct comparison is not possible. The only way would be to apply both approaches on the same data set.

6. Conclusions

Our study brings strong arguments for distinguishing peaks of autochthonous turbidity from allochthonous ones. Hydraulics of flow within the epiphreatic zone appear to be the main source of autochthonous turbidity, when flow velocity and shear stress are the highest. This usually takes place during the rising and the recession of the flooding of epiphreatic conduits (i.e., of the spring discharge). During the paroxysm of the flood event, epiphreatic conduits are flooded and the flow velocity decreases as the flow cross section increases. Allochthonous turbidity usually produces peaks which are longer and more delayed. Their turbidity is characterized by thinner particles (0.9–1.5 μm), higher *E. coli* concentrations, and higher UV fluorescence than that of autochthonous turbidity.

As turbidity peaks represent a serious issue for drinking water resources, this knowledge will certainly help improve the management of water supply. We believe that information provided here is a significant step for improving the prediction of the time of arrival, the intensity and the characteristics of turbidity in karst springs. As allochthonous turbidity is strongly related to the arrival of pollutions from sources within the catchment area, the recognition and prediction of these arrivals is an interesting input for managing water.

Data Availability Statement

The data analyzed in this study can be downloaded at: https://doi.org/10.4211/hs.f73f2de9b7fc484faad7827c9534ff56 (Vuilleumier et al., 2020). The numerical model and simulation results can be downloaded at: https://doi.org/10.4211/hs.c647e1fab5874f29bf2e92f56f3e1f94 (Vuilleumier, 2019).

Acknowledgments
Some of the measurements analyzed in this study have been supported by the A16 highway project of the FEDRO (Federal Roads Office) and the Canton of Jura within a contract with MFR Géologie-Géotechnique SA and RWB Jura SA. The authors are grateful to them for making these data available. Special thanks to the FEDRO and the Canton of Jura for their open and pragmatic approach in dealing with this challenging issue and committing the necessary financial resources, which greatly contributed to this study. The Spéléo-Club Jura and its president Pierre Xavier Meury have also been supportive of our research and made access to the cave possible under good conditions. The authors also thank the associate editor Christophe Ancey and the reviewers Andrew Luhmann and Max Cooper for their helpful comments. Open Access Funding provided by Universite de Neuchatel.

References

Atteia, O., & Kozel, R. (1997). Particle size distributions in waters from a karstic aquifer: From particles to colloids. *Journal of Hydrology*, *201*(1), 102–119. https://doi.org/10.1016/S0022-1694(97)00033-4

Auckenthaler, A., Raso, G., & Huggenberger, P. (2002). Particle transport in a karst aquifer: Natural and artificial tracer experiments with bacteria, bacteriophages and microspheres. *Water Science and Technology*, *46*(3), 131–138. https://doi.org/10.2166/wst.2002.0072

Bögli, A. (1980). *Karst hydrology and physical speleology*. Springer-Verlag. Retrieved from https://www.springer.com/gp/book/9783642676710

Chen, Z., & Goldscheider, N. (2014). Modeling spatially and temporally varied hydraulic behavior of a folded karst system with dominant conduit drainage at catchment scale, Hochifen–Gottesacker, Alps. *Journal of Hydrology*, *514*, 41–52. https://doi.org/10.1016/j.jhydrol.2014.04.005

Dogwiler, T., & Wicks, C. M. (2004). Sediment entrainment and transport in fluviokarst systems. *Journal of Hydrology*, *295*(1–4), 163–172. https://doi.org/10.1016/j.jhydrol.2004.03.002

Favre, I. (2001). *Base de données des essais de traçage du plateau karstique de Bure (JU), SIG, interprétations statistiques* (Master's thesis). University of Neuchâtel. Retrieved from http://data.rero.ch/01-R005501844/html?view=NJ_V1

Fournier, M., Massei, N., Bakalowicz, M., & Dupont, J.-P. (2007). Use of univariate clustering to identify transport modalities in karst aquifers. *Comptes Rendus Geoscience*, *339*(9), 622–631. https://doi.org/10.1016/j.crte.2007.07.009

Fournier, M., Massei, N., Bakalowicz, M., Dussart-Baptista, L., Rodet, J., & Dupont, J. P. (2007). Using turbidity dynamics and geochemical variability as a tool for understanding the behavior and vulnerability of a karst aquifer. *Hydrogeology Journal*, *15*(4), 689–704. https://doi.org/10.1007/s10040-006-0116-2

Gabrovšek, F., Peric, B., & Kaufmann, G. (2018). Hydraulics of epiphreatic flow of a karst aquifer. *Journal of Hydrology*, *560*, 56–74. https://doi.org/10.1016/j.jhydrol.2018.03.019

Gale, S. J. (1984). The hydraulics of conduit flow in carbonate aquifers. *Journal of Hydrology*, *70*(1–4), 309–327. https://doi.org/10.1016/0022-1694(84)90129-X

Gigon, R., & Wenger, R. (1986). *Inventaire spéléologique de la Suisse. Tome II*. Commission de Spéléologie de la Société helvétique des Sciences naturelles.

Grasso, D. A., & Jeannin, P.-Y. (1994). Estimation des pertes dans la partie aval du réseau karstique de la Milandrine: Bilan hydrique au sein d'un aquifère karstique. *Bulletin d'Hydrogeologie*, *13*, 115–128.

Gunn, J., Tranter, J., Perkins, J., & Hunter, C. (1997). *Sanitary bacterial dynamics in a mixed karst aquifer* (Vol. 247, pp. 61–71). IAHS Publications-Series of Proceedings and Reports-Intern Assoc Hydrological Sciences. Retrieved from http://hydrologie.org/redbooks/a247/iahs_247_0061.pdf

Herman, E. K., Toran, L., & White, W. B. (2008). Threshold events in spring discharge: Evidence from sediment and continuous water level measurement. *Journal of Hydrology*, *351*(1–2), 98–106. https://doi.org/10.1016/j.jhydrol.2007.12.001

Herman, E. K., Toran, L., & White, W. B. (2012). Clastic sediment transport and storage in fluviokarst aquifers: An essential component of karst hydrogeology. *Carbonates and Evaporites*, *27*(3–4), 211–241. https://doi.org/10.1007/s13146-012-0112-7

Jeannin, P.-Y. (2001). Modeling flow in phreatic and epiphreatic karst conduits in the Hölloch Cave (Muotatal, Switzerland). *Water Resources Research*, *37*(2), 191–200. https://doi.org/10.1029/2000WR900257

Kaufmann, G., Gabrovšek, F., & Turk, J. (2016). Modelling cave flow hydraulics in Postojnska jama, Slovenia. *Acta Carsologica*, *45*, 57–70. https://doi.org/10.3986/ac.v45i1.3059

Knierim, K. J., Hays, P. D., & Bowman, D. (2015). Quantifying the variability in Escherichia coli (E. coli) throughout storm events at a karst spring in northwestern Arkansas, United States. *Environmental Earth Sciences*, *74*(6), 4607–4623. https://doi.org/10.1007/s12665-015-4416-5

Kovács, A., & Jeannin, P.-Y. (2003). Hydrogeological overview of the Bure plateau, Ajoie, Switzerland. *Eclogae Geologicae Helvetiae*, *96*(3), 367–380. https://doi.org/10.1007/s00015-003-1099-9

Lacroix, M., Rodet, J., Wang, H. Q., Massei, N., & Dupont, J.-P. (2000). Origine des matières en suspension dans un système aquifère karstique: Apports de la microgranulométrie. *Comptes Rendus de l'Academie des Sciences—Series IIA: Earth and Planetary Science*, *330*(5), 347–354. https://doi.org/10.1016/S1251-8050(00)00161-0

Mahler, B. J., & Lynch, F. L. (1999). Muddy waters: Temporal variation in sediment discharging from a karst spring. *Journal of Hydrology*, *214*(1–4), 165–178. https://doi.org/10.1016/S0022-1694(98)00287-X

Mahler, B. J., Lynch, L., & Bennett, P. C. (1999). Mobile sediment in an urbanizing karst aquifer: Implications for contaminant transport. *Environmental Geology*, *39*(1), 25–38. https://doi.org/10.1007/s002540050434

Massei, N., Wang, H., Dupont, J., Rodet, J., & Laignel, B. (2003). Assessment of direct transfer and resuspension of particles during turbid floods at a karstic spring. *Journal of Hydrology*, *275*(1–2), 109–121. https://doi.org/10.1016/S0022-1694(03)00020-9

Palmer, A. N., & Palmer, M. V. (2006). Hydraulic processes in the origin of tiankengs. *Speleogenesis and Evolution of Karst Aquifers*, *4*(1), 1–8.

Pantillon, P. (1993). *Etude hydrogéologique du site expérimental du Maira dans le projet COST 65* (Unpublished master's thesis). University of Neuchâtel.

Pasquarell, G. C., & Boyer, D. G. (1995). Agricultural impacts on bacterial water quality in karst groundwater. *Journal of Environmental Quality*, *24*(5), 959–969. https://doi.org/10.2134/jeq1995.00472425002400050026x

Perrin, J. (2003). *A conceptual model of flow and transport in a karst aquifer based on spatial and temporal variations of natural tracers* (Unpublished doctoral dissertation). Université de Neuchâtel.

Perrin, J., Jeannin, P.-Y., & Cornaton, F. (2007). The role of tributary mixing in chemical variations at a karst spring, Milandre, Switzerland. *Journal of Hydrology*, *332*(1–2), 158–173. https://doi.org/10.1016/j.jhydrol.2006.06.027

Perrin, J., Jeannin, P.-Y., & Zwahlen, F. (2003). Epikarst storage in a karst aquifer: A conceptual model based on isotopic data, Milandre test site, Switzerland. *Journal of Hydrology*, *279*(1–4), 106–124. https://doi.org/10.1016/S0022-1694(03)00171-9

Pronk, M. (2008). *Origin and behaviour of microorganisms and particles in selected karst aquifer systems* (Unpublished doctoral dissertation). University of Neuchâtel.

Pronk, M., Goldscheider, N., & Zopfi, J. (2006). Dynamics and interaction of organic carbon, turbidity and bacteria in a karst aquifer system. *Hydrogeology Journal*, *14*(4), 473–484. https://doi.org/10.1007/s10040-005-0454-5

Pronk, M., Goldscheider, N., & Zopfi, J. (2007). Particle-size distribution as indicator for fecal bacteria contamination of drinking water from karst springs. *Environmental Science & Technology*, *41*(24), 8400–8405. https://doi.org/10.1021/es071976f

Reed, T. M., McFarland, J. T., Fryar, A. E., Fogle, A. W., & Taraba, J. L. (2010). Sediment discharges during storm flow from proximal urban and rural karst springs, central Kentucky, USA. *Journal of Hydrology*, *383*(3–4), 280–290. https://doi.org/10.1016/j.jhydrol.2009.12.043

Rodriguez, A. (1996). *Le transport des particules dans le karst: Étude préliminaire dans le karst jurassien* (Unpublished master's thesis). University of Neuchâtel.

Ryan, M., & Meiman, J. (1996). An examination of short-term variations in water quality at a karst spring in Kentucky. *Ground Water*, *34*(1), 23–30. https://doi.org/10.1111/j.1745-6584.1996.tb01861.x

Schiperski, F., Zirlewagen, J., Hillebrand, O., Licha, T., & Scheytt, T. (2015). Preliminary results on the dynamics of particles and their size distribution at a karst spring during a snowmelt event. *Journal of Hydrology*, *524*, 326–332. https://doi.org/10.1016/j.jhydrol.2015.02.035

Schiperski, F., Zirlewagen, J., Hillebrand, O., Nödler, K., Licha, T., & Scheytt, T. (2015). Relationship between organic micropollutants and hydro-sedimentary processes at a karst spring in south-west Germany. *Science of the Total Environment*, *532*, 360–367. https://doi.org/10.1016/j.scitotenv.2015.06.007

Schroeder, J., & Ford, D. C. (1983). Clastic sediments in Castleguard Cave, Columbia Icefields, Alberta, Canada. *Arctic and Alpine Research*, *15*, 451–461. https://doi.org/10.2307/1551232

Valdes, D., Dupont, J.-P., Massei, N., Laignel, B., & Rodet, J. (2006). Investigation of karst hydrodynamics and organization using autocorrelations and t-c curves. *Journal of Hydrology*, *329*(3–4), 432–443. https://doi.org/10.1016/j.jhydrol.2006.02.030

Vesper, D. J., & White, W. B. (2003). Metal transport to karst springs during storm flow: An example from Fort Campbell, Kentucky/Tennessee, USA. *Journal of Hydrology*, *276*(1–4), 20–36. https://doi.org/10.1016/S0022-1694(03)00023-4

Vuilleumier, C. (2017). *Hydraulics and sedimentary processes in the karst aquifer of Milandre (Jura Mountains, Switzerland)* (Doctoral dissertation). Université de Neuchâtel. Retrieved from http://doc.rero.ch/record/306843

Vuilleumier, C. (2019). *SWMM model of the Milandre Cave (Switzerland)*. HydroShare. https://doi.org/10.4211/hs.c647e1fab5874f29bf2e92f56f3e1f94

Vuilleumier, C., Jeannin, P.-Y., & Hessenauer, M. (2020). *Monitoring of suspended particles in the Milandre karst system (Switzerland)*. HydroShare. https://doi.org/10.4211/hs.f73f2de9b7fc484faad7827c9534ff56

Vuilleumier, C., Jeannin, P. Y., & Perrochet, P. (2019). Physics-based fine-scale numerical model of a karst system (Milandre Cave, Switzerland). *Hydrogeology Journal*, *27*(7), 2347–2363. https://doi.org/10.1007/s10040-019-02006-y

Wu, Y., Jiang, Y., Yuan, D., & Li, L. (2008). Modeling hydrological responses of karst spring to storm events: Example of the Shuifang spring (Jinfo Mt., Chongqing, China). *Environmental Geology*, *55*(7), 1545–1553. https://doi.org/10.1007/s00254-007-1105-z